Front. Chem. Sci. Eng. 2022, 16(12): 1782−1792
https://doi.org/10.1007/s11705-022-2220-9

RESEARCH ARTICLE

Room-temperature hydrogenation of halogenated nitrobenzenes over metal–organic-framework-derived ultra-dispersed Ni stabilized by N-doped carbon nanoneedles

Yuemin Lin[1], Yuanyuan Zhang[1], Renfeng Nie (✉)[2], Kai Zhou[1], Yao Ma[1], Mingjie Liu[1], Dan Lu[1], Zongbi Bao[1,3], Qiwei Yang[1,3], Yiwen Yang[1,3], Qilong Ren[1,3], Zhiguo Zhang (✉)[1,3]

1 Key Laboratory of Biomass Chemical Engineering of Ministry of Education, College of Chemical and Biological Engineering, Zhejiang University, Hangzhou 310027, China
2 School of Chemical Engineering, Henan Center for Outstanding Overseas Scientists, Zhengzhou University, Zhengzhou 450001, China
3 Institute of Zhejiang University—Quzhou, Quzhou 324000, China

© Higher Education Press 2022

Abstract Ultra-dispersed Ni nanoparticles (7.5 nm) on nitrogen-doped carbon nanoneedles (Ni@NCNs) were prepared by simple pyrolysis of Ni-based metal–organic-framework for selective hydrogenation of halogenated nitrobenzenes to corresponding anilines. Two different crystallization methods (stirring and static) were compared and the optimal pyrolysis temperature was explored. Ni@NCNs were systematically characterized by wide analytical techniques. In the hydrogenation of *p*-chloronitrobenzene, Ni@NCNs-600 (pyrolyzed at 600 °C) exhibited extraordinarily high performance with 77.9 h^{-1} catalytic productivity and > 99% *p*-chloroaniline selectivity at full *p*-chloronitrobenzene conversion under mild conditions (90 °C, 1.5 MPa H_2), showing obvious superiority compared with reported Ni-based catalysts. Notably, the reaction smoothly proceeded at room temperature with full conversion and > 99% selectivity. Moreover, Ni@NCNs-600 afforded good tolerance to various nitroarenes substituted by sensitive groups (halogen, nitrile, keto, carboxylic, etc.), and could be easily recycled by magnetic separation and reused for 5 times without deactivation. The adsorption tests showed that the preferential adsorption of $–NO_2$ on the catalyst can restrain the dehalogenation of *p*-chloronitrobenzene, thus achieving high *p*-chloroaniline selectivity. While the high activity can be attributed to high Ni dispersion, special morphology, and rich pore structure of the catalyst.

Keywords halogenated nitrobenzenes, room-temperature hydrogenation, Ni nanoparticles, nitrogen-doped carbon nanoneedles, metal–organic-framework

Received May 28, 2022; accepted July 4, 2022

E-mails: rnie@zzu.edu.cn (Nie R.), zhiguo.zhang@zju.edu.cn (Zhang Z.)

1 Introduction

Catalytic hydrogenation of nitroarenes to amines is an important chemical transformation in industry, widely applied in the manufacture of pharmaceuticals, dyes, macromolecules, and so on [1]. In view of the principles of green and sustainable chemistry, developing heterogeneous catalysts with high performance for nitroarenes reduction is highly desirable.

Catalysts based on noble metals, especially Pd and Pt, have shown high activity but unsatisfactory selectivity when confronting substrates containing halogen substituents or other reducible groups [2–4]. In addition, the high cost and limited availability of noble metals are long-term problems in industry. Comparatively, developing earth-abundant metals (e.g., Ni, Co and Fe) is important and continues to attract scientific interests. However, non-noble metal catalysts often require harsh conditions (e.g., high temperature, high H_2 pressure) to achieve desired conversion [5,6], which results in uncontrollable side reactions.

Recently, designing non-noble metal catalysts with high activity has attracted researchers' great attention. Typically, conventional catalyst preparation includes metal salts loading on selected support via impregnation or co-precipitation, followed by thermal or chemical reduction [7–9]. Unfortunately, these methods often result

in uneven metal dispersion due to severe sintering, limiting the catalyst activity and selectivity. Even worse, owing to the weak metal-support interactions, these catalysts usually suffer from severe metal leaching or agglomeration in catalytic process and low resistance to oxidation in air [10,11]. Therefore, it is desirable to synthesize highly dispersed and stable non-noble metal catalysts for selective hydrogenation of nitroarenes under mild conditions.

In the past decades, porous carbons have demonstrated great potential in catalysis due to their exceptional chemical and thermal stability, high surface area, and electronic conductivity [12,13]. Particularly, N-doped carbons have emerged as promising supports of heterogeneous catalysts [14,15]. Growing evidence suggests that N dopants can stabilize metal nanoparticles by forming M–N species and thereby enhance the catalytic performance [14,16]. Metal–organic-frameworks (MOFs), a new class of crystalline materials assembled by metal ions and organic ligands, are fascinating sacrificial precursors for the synthesis of porous carbon catalysts [17–21]. Compared with the conventional methods, MOF-derived carbons avoid the use of templates for pore-forming and toxic acids for template removal [22]. Despite numerous MOF-derived carbon catalysts have been developed, several common defects still exist: (1) micropore-dominated pore structure limits the substrate diffusion, (2) the irreversible sintering of metal (particle sizes > 10 nm) limits its exposure, and (3) the structural evolution is uncontrollable [23]. In addition, nitrogen dopants are mostly introduced via the carbonization of zeolitic imidazolate frameworks [24,25]. Consequently, further efforts are still expected to develop efficient nitrogen-doped carbon catalysts derived from novel MOFs.

Based on the abovementioned considerations, herein, we developed a stirring-crystallization method for the preparation of nanoneedle-like di-ligand Ni-MOF. After pyrolysis at 400–700 °C, ultra-dispersed Ni nanoparticles stabilized by N-doped carbon nanoneedles (Ni@NCNs) were successfully prepared. Under optimized conditions, the optimal catalyst (Ni@NCNs-600) achieved excellent performance in the hydrogenation of *p*-chloronitrobenzene under low temperature and H_2 pressure. Moreover, Ni@NCNs-600 afforded remarkable tolerance to various functionalized nitroarenes, easy magnetic separation and outstanding reusability.

2 Experimental

2.1 Materials

Terephthalic acid (99%) and 4,4'-bipyridine (98%) were purchased from Macklin, China. $Ni(NO_3)_2 \cdot 6H_2O$ (≥ 98%), ethanol (≥ 99.5%), and *N*,*N*-dimethylformamide (DMF, ≥ 99.5%) were purchased from Sinopharm Chemical Reagent Co. Ltd., China. *p*-Chloronitrobenzene (> 99.5%), *o*-chloronitrobenzene (> 99%), *m*-chloronitrobenzene (99%), *o*-bromonitrobenzene (99%), *p*-bromonitrobenzene (> 99.0%), *p*-iodonitrobenzene (98%), and 4-nitrobenzoic acid (99%) were purchased from Aladdin Chemicals. 4-Nitrobenzonitrile (97%) and 4-nitroacetophenone (99.91%) were purchased from Bidepharm. 2,5-Dibromonitrobenzene (98%) was purchased from TCI. All chemicals were used as received without any further treatment.

2.2 Catalyst preparation

Synthesis of Ni-$MOF_{stirring}$. Generally, terephthalic acid (0.83 g, 5.0 mmol), 4,4'-bipyridine (0.39 g, 2.5 mmol), and $Ni(NO_3)_2 \cdot 6H_2O$ (1.45 g, 5.0 mmol) were dissolved in 100 mL DMF to form a clear solution. Then, the mixture was heated to 100 °C and crystallized under stirring for 48 h. Green precipitate was isolated by centrifugation and washed with DMF and ethanol for three times, respectively. After drying overnight, green powder crystal was successfully obtained, which was denoted as Ni-$MOF_{stirring}$ (750 mg).

Synthesis of Ni-MOF_{static}. Generally, terephthalic acid (0.83 g, 5.0 mmol), 4,4'-bipyridine (0.39 g, 2.5 mmol), and $Ni(NO_3)_2 \cdot 6H_2O$ (1.45 g, 5.0 mmol) were dissolved in 100 mL DMF to form a clear solution. The mixture was sealed in a Teflon-lined stainless-steel autoclave (200 mL) and transferred to a 100 °C oven for 48 h. Green precipitate was isolated by centrifugation and washed with DMF and ethanol for three times, respectively. After drying overnight, green powder crystal was successfully obtained, which was denoted as Ni-MOF_{static} (646 mg).

Preparation of Ni@NCNs-T and Ni@NCNs-600-static catalysts. Typically, 300 mg Ni-$MOF_{stirring}$ was placed in a porcelain boat and transferred to a tube furnace. Under an argon flow (100 $mL \cdot min^{-1}$), the furnace was heated to target temperature with a ramping rate of 5 $°C \cdot min^{-1}$ and held for 2 h. After naturally cooling down to room temperature, the black powder Ni@NCNs-T was obtained, where T represents the pyrolysis temperature. The preparation of Ni@NCNs-600-static was similar as that of Ni@NCNs-600 except for using Ni-MOF_{static} as precursor.

2.3 Characterizations

The powder X-ray diffraction (PXRD) patterns were obtained using a PANalytical X'Pert PRO diffractometer with Cu Kα radiation operated at 40 kV, 40 mA. Thermogravimetric analysis (TGA) was conducted on SDT 650 instrument under a 100 $mL \cdot min^{-1}$ flow of N_2, ramping from 50 to 800 °C at a rate of 10 $°C \cdot min^{-1}$. N_2 physisorption analysis was performed on a Micromeritics 3Flex 3.01 instrument at 77 K. CO_2 physisorption

analysis was performed on an Autosorb-IQ-MP instrument at 195 K. The inductively coupled plasma optical emission spectrometry (ICP-OES) was conducted on a Varian-730ES atomic absorption spectrometer to determine the loading of nickel. The samples for ICP-OES measurement were digested by calcination at 550 °C for 6 h and following dissolution in hot aqua regia. Elemental analysis results were achieved on the Elementar Vario MICRO elemental analyzer. The Raman spectrum was collected on a LabRam HR evolution. Scanning electron microscopy (SEM) images were recorded on SUPRA55. Transmission electron microscope (TEM) and EDS mapping were conducted on FEI Tecnai G2 F20 at an accelerating voltage of 200 kV. The X-ray photoelectron spectroscopy (XPS) measurements were performed on a Thermo Scientific K-Alpha analyzer with an Al Kα (1486.6 eV) X-ray source, and the binding energy was calibrated by the C 1s peak (284.8 eV). CasaXPS was used to process raw data files.

2.4 Adsorption test

For the adsorption test of nitrobenzene, 500 ppm (10^{-6}) nitrobenzene in ethanol solution was prepared. Next, 5 mL solution was mixed with 50 mg Ni@NCNs-600 and stirred at room temperature. After 4 h, the mixture was centrifuged and a certain amount of supernatant was diluted with ethanol. The as-prepared solution was analyzed by an ultraviolet–visible (UV–vis, Shimadzu UV-2600). The capacity of nitrobenzene adsorption was calculated via the equation: the capacity of nitrobenzene adsorption = $\frac{(c_0 - c_r) \times V_0}{m_c}$. Here, c_0 and c_r are the initial concentration and the residual of nitrobenzene, V_0 is the volume of ethanol solution, m_c is the mass of Ni@NCNs-600 catalyst. The procedure was identical for the adsorption test of chlorobenzene and *p*-chloronitrobenzene.

2.5 Catalytic studies

Hydrogenation reaction was carried out in a stainless-steel reactor equipped with a magnetic stirrer. Typically, 53 mg *p*-chloronitrobenzene, 2.8 wt % equiv. catalyst, 2 mL solvent were added into the reactor. The reactor was purged with H_2 for 5 times, pressurized to desired pressure, and heated at desired temperature under stirring of 500 r·min^{-1}. After a certain time, the reaction was quickly quenched in cold water. The catalyst was separated by magnet and the solution was analyzed by gas chromatography (GC Shimadzu 2010) equipped with a WondaCap-5 column (30 m × 0.25 mm × 0.25 μm) and a flame ionization detector. The identification of products was conducted by NMR (Bruker Avance III 400 MHz).

3 Results and discussion

3.1 Catalyst characterizations

As illustrated in Fig. 1, Ni-MOF was synthesized first with terephthalic acid and 4,4'-bipyridine as di-ligands and nickel(II) nitrate as Ni source (Fig. 1(a)). The mass yield of stirring-crystallization was 50%, which was higher than that using static-crystallization (43%). PXRD patterns (Fig. 1(b)) of Ni-MOF$_{stirring}$ and Ni-MOF$_{static}$ show similar peak diffractions. SEM images (Fig. 2) reveal that Ni-MOF$_{stirring}$ presents slender needle crystals with small thickness and length (0.2 μm × 1.9 μm), while Ni-MOF$_{static}$ presents thick rod crystals with a much larger size (2.6 μm × 7.6 μm).

In Fig. S1 (cf. Electronic Supplementary Material, ESM), TGA measurement shows that the weight loss of Ni-MOF$_{stirring}$ went through three steps, including solvent removal (3.5%), ligands degradation (50.1%) and gradual loss of C/N after 435 °C. Therefore, four different pyrolysis temperatures (400, 500, 600, and 700 °C) were selected for Ni@NCNs-T preparation.

The crystalline structure of Ni@NCNs-T was determined by PXRD shown in Fig. 3. Figure 3(a) reveals that the characteristic peaks of Ni-MOF disappear in Ni@NCNs-T, indicating full decomposition of MOF

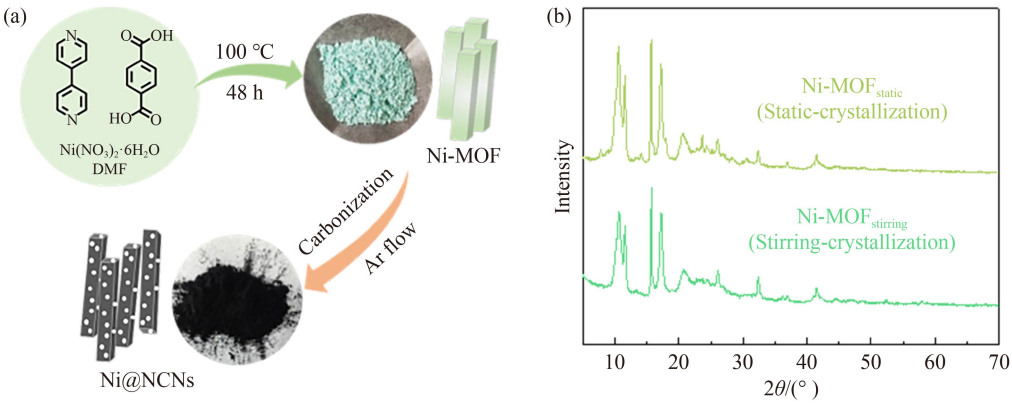

Fig. 1 (a) Illustration for preparation of Ni@NCNs-T; (b) PXRD patterns of Ni-MOFs by different preparation methods.

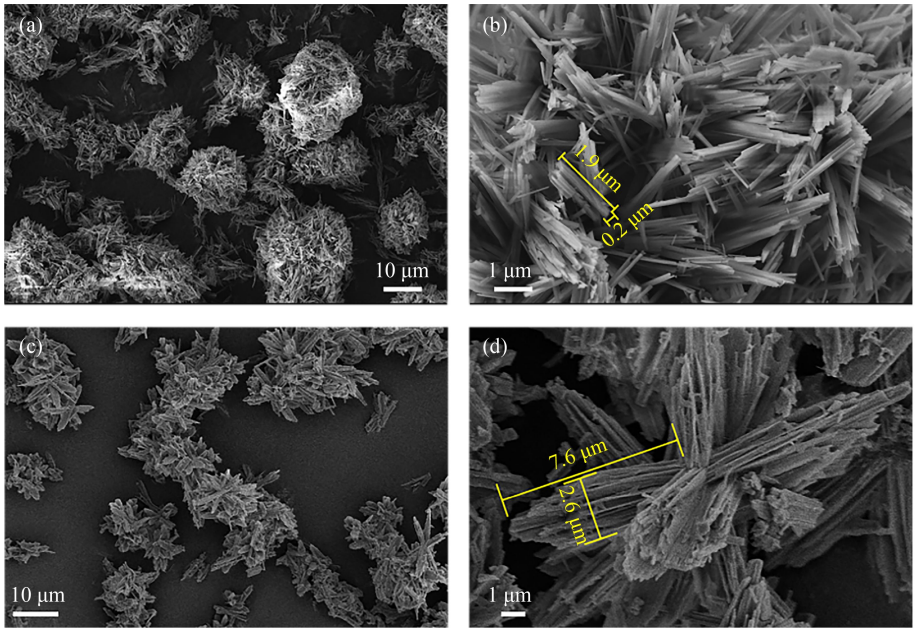

Fig. 2 SEM images of Ni-MOFs prepared by (a, b) stirring-crystallization and (c, d) static-crystallization.

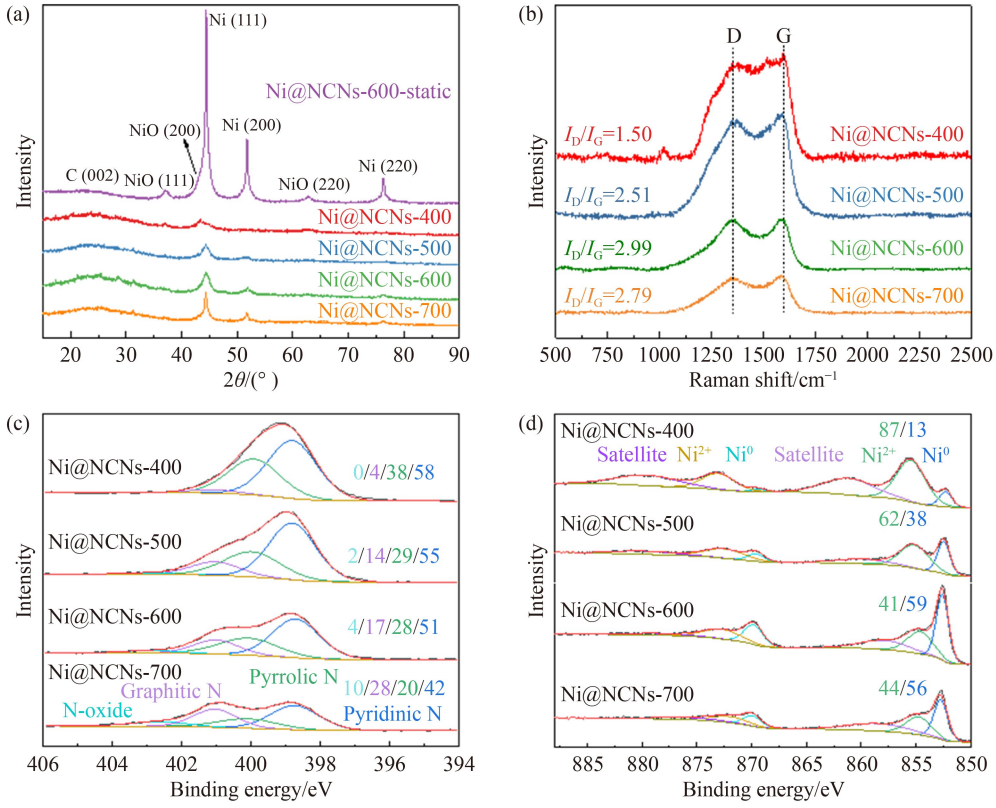

Fig. 3 (a) PXRD patterns, (b) Raman spectra, (c) N 1s and (d) Ni 2p XPS spectra of Ni@NCNs.

precursor. Weak diffraction at 25° is attributed to C (002) plane of graphitic carbon [26,27]. Peaks at 37.1°, 43.3° and 62.9° correspond to the characteristic diffractions of NiO (111), (200) and (220) lattice planes, respectively [28,29]. Peaks at 44.5°, 51.8° and 76.4° are ascribed to metallic Ni (111), (200) and (220) lattice planes, respectively [30]. As for Ni@NCNs-400, NiO is the dominant phase and weak metallic Ni diffractions are observed. As increasing the pyrolysis temperature, NiO phase weakens but metallic Ni strengthens. Only metallic Ni diffractions are observed for Ni@NCNs-500 and Ni@NCNs-600. Nevertheless, weak NiO diffractions reappear in Ni@NCNs-700, because nitrogen loss triggered the reconstitution of Ni–O. As calculated by

Debye–Scherrer equation, the crystalline sizes of Ni in Ni@NCNs-500, Ni@NCNs-600, and Ni@NCNs-700 are around 6.7, 7.0, and 10.9 nm, respectively, revealing that Ni nanoparticles tend to agglomerate at higher temperature. In addition, compared with Ni@NCNs-600, Ni@NCNs-600-static shows much sharper Ni and NiO diffractions, and the crystalline Ni size is calculated to be 10.8 nm.

Nitrogen adsorption–desorption isotherms (Fig. S2, cf. ESM) show that Ni@NCNs-T displays a typical type IV curve, revealing the coexistence of mesopores and micropores. Compared with Ni-MOF$_{stirring}$ (Fig. S3, cf. ESM), Ni@NCNs-T exhibits higher surface area and pore volume (Table S1, cf. ESM), which is beneficial to the mass transfer in catalytic reaction. For example, the surface area and pore volume of Ni@NCNs-600 (359.8 $m^2 \cdot g^{-1}$, 0.45 $cm^3 \cdot g^{-1}$) are almost 2 and 3 times of Ni-MOF$_{stirring}$ (176.1 $m^2 \cdot g^{-1}$, 0.14 $cm^3 \cdot g^{-1}$), respectively.

Raman spectra (Fig. 3(b)) show that all samples display two predominant peaks corresponding to D band (~1357 cm^{-1}) and G band (~1585 cm^{-1}). The relative ratio of D to G band (I_D/I_G) reflects the degree of carbon defects [31]. The I_D/I_G ratio first increases and then decreases with the increase of pyrolysis temperature. The highest I_D/I_G ratio (2.99) is achieved for Ni@NCNs-600, indicating its rich defects of the carbon skeleton.

As measured by elemental analysis and ICP-OES (Table S2, cf. ESM), both C and N contents decrease, while Ni content increases (47–59 wt %) as increasing pyrolysis temperature. N 1s XPS spectra of Ni@NCNs-T (Fig. 3(c)) can be deconvoluted into four peaks at 398.8, 400.0, 401.0, and 402.8 eV, corresponding to pyridinic N, pyrrolic N, graphitic N, and N-oxide, respectively [32,33]. As increasing pyrolysis temperature, pyridinic and pyrrolic N species decrease significantly, while graphitic N and N-oxide species increase. Ni 2p XPS spectra (Fig. 3(d)) show that, as increasing the pyrolysis temperature, the content of Ni^0 increases and reaches the maximum (59%) for Ni@NCNs-600, then decreases to 56% for Ni@NCNs-700. These results demonstrate that Ni species in Ni-MOF can be *in situ* reduced, while the low Ni^0 content of Ni@NCNs-700 is attributed to the reconstruction of Ni–O bond caused by nitrogen loss [34]. Wide XPS survey spectra show that high pyrolysis temperature results in less Ni exposure (Fig. S4, Table S3, cf. ESM), attributing to the formation of Ni@C core-shell structure [35].

Considering the excellent activity of Ni@NCNs-600 as referred to later, its morphology was surveyed by SEM and TEM (Fig. 4). SEM images (Figs. 4(a–c)) show that Ni@NCNs-600 presents nest-like accumulations woven by carbon nanoneedles decorated with Ni nanoparticles, which is similar as that of parent Ni-MOF$_{stirring}$. TEM images (Figs. 4(d) and 4(e)) confirm the presence of ultra-highly dispersed Ni nanoparticles on carbon nanoneedles, and the average Ni size is measured to be 7.5 nm (Fig. 4(e)), agreeing with the PXRD results (Fig. 3(a)). Notably, such high Ni dispersion is rare and challenging for catalysts with ultra-high Ni loading (51 wt %, Table S2), suggesting that N-doping can improve the dispersion of Ni nanoparticles. The lattice spacing in Fig. 4(f) is measured to be 0.204 nm, attributing to Ni (111) plane [29]. The selected area electron diffraction (SEAD) patterns (Fig. 4(f)) show the diffraction rings of metallic Ni (111) and Ni (200) planes [36]. Elemental mapping (Fig. 4(g)) further reveals that the elements of C, N, and Ni are evenly distributed throughout the carbon nanoneedles. Comparatively, Ni nanoparticles in Ni@NCNs-600-static are also well dispersed, but the Ni size (9.3 nm) is larger than that of Ni@NCNs-600 (Figs. 4(e) and 4(i)). These results suggest that the unique crystal morphology of MOF precursor can restrain Ni sintering, thus predictably exhibiting good performance in catalytic hydrogenation.

3.2 Catalytic performance

Selective hydrogenation of *p*-chloronitrobenzene was chosen as a model reaction to evaluate the catalyst performance (Fig. 5). The main side reactions include the formation of intermediates and the dehalogenation of *p*-chloroaniline (Fig 5(a)). The activity and selectivity of Ni@NCNs-T were strongly influenced by the pyrolysis temperature (Fig. 5(b)). Nearly no products were observed for Ni-MOF precursor, excluding the catalysis of Ni^{2+} and ligands. With Ni@NCNs-400 as catalyst, 18.0% *p*-chloronitrobenzene conversion was achieved, while no *p*-chloroaniline except for intermediates (e.g., azoxybenzene) were observed. As for Ni@NCNs-500, *p*-chloronitrobenzene conversion increased remarkably to 93.8% and the *p*-chloroaniline selectivity achieved 89.9%, attributing to the increased Ni^0 content in catalyst. When increasing pyrolysis temperature to 600 °C, the conversion and *p*-chloroaniline selectivity further increased to 100% and 95.5%, respectively, in which no dehalogenated product (e.g., aniline) was detected. However, further increasing pyrolysis temperature to 700 °C decreased the conversion and *p*-chloroaniline selectivity to 59.4% and 51.4%, respectively, ascribing to severe sintering of Ni nanoparticles and pore collapse of the catalyst. This phenomenon suggested that the dramatic decrease of nitrogen under 700 °C resulted in Ni aggregation and weaker metal-support interactions, decreasing the catalytic activity. Moreover, Ni@NCNs-600-static originating from static-crystallized Ni-MOF achieved 95.5% conversion and 81.0% *p*-chloroaniline selectivity, highlighting the advantage of stirring-crystallization for the preparation of Ni-MOF and corresponding carbon-based catalysts (Fig. 5(b)). When the substrate concentration was scaled up to 14.8 times (5 mmol), full conversion along with > 99% *p*-chloroaniline selectivity was achieved at 60 min under the

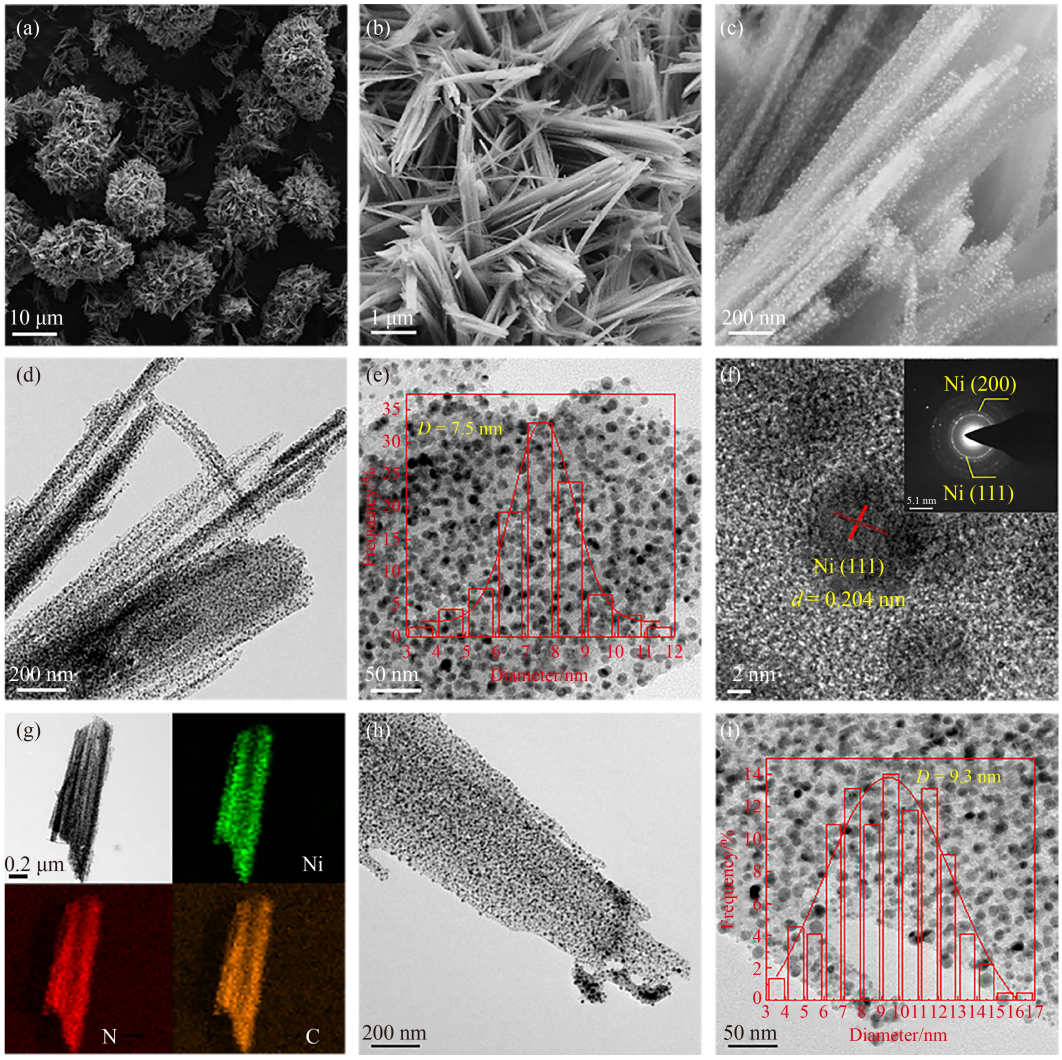

Fig. 4 (a, b, c) SEM images of Ni@NCNs-600 at different nanoscales; (d, e) TEM images; (f) high resolution TEM image and SEAD patterns; (g) elemental mapping images of Ni@NCNs-600; (h, i) TEM images of Ni@NCNs-600-static. The insets in (e) and (i) show the size distributions of Ni nanoparticles.

optimized conditions as referred to later (Fig. 5(b)). The superior performance of Ni@NCNs-600 encouraged us to investigate the reason of high *p*-chloroaniline selectivity. UV−vis spectra showed that the adsorption amounts of nitrobenzene and *p*-chloronitrobenzene are much higher than that of chlorobenzene (Fig. 5(c)), suggesting that the preferential adsorption of $–NO_2$ over –Cl can restrain the dechlorination of the desired product. Compared with other reported Ni-based catalysts (Fig. 5(d), Table S4, cf. ESM) [31,37–45], Ni@NCNs-600 presents extraordinary superiority with high catalytic productivity of 77.9 h^{-1} and > 99% *p*-chloroaniline selectivity under mild conditions (90 °C, 1.5 MPa H_2). According to previous characterizations, the superior performance of Ni@NCNs-600 can be ascribed to the following reasons: (1) higher content of Ni^0; (2) ultra-high dispersion of Ni nanoparticles; (3) uniform morphology of nanoneedles; (4) oriented adsorption of $–NO_2$.

The reaction conditions were further optimized (Fig. 6). Considering water can promote $–NO_2$ hydrogenation due to its bond polarization and H-shuttling effects [46–48], the influence of water content was studied with the optimal Ni@NCNs-600 (Fig. 6(a)). It was found that ethanol achieved only 69.6% conversion and 63.5% *p*-chloroaniline selectivity at 30 min. Interestingly, replacing ethanol with 20% water, the conversion and *p*-chloroaniline selectivity increased to 100% and 98.4%, respectively. N-doping improved the catalyst hydrophilicity, which favored the dispersion of Ni@NCNs-600 in ethanol/H_2O mixed solvent. Further increasing water content from 40% to 100%, the reaction rate decelerated slightly, while the *p*-chloroaniline selectivity decreased dramatically from 99.4% to 72.2%, ascribing to low substrate solubility in the presence of high content of water.

With optimal ethanol/H_2O (8/2) as solvent, the effect of reaction temperature was further investigated in Fig. 6(b). Fixing reaction time at 20 min, only 27.4% conversion and 26.6% *p*-chloroaniline selectivity were achieved at

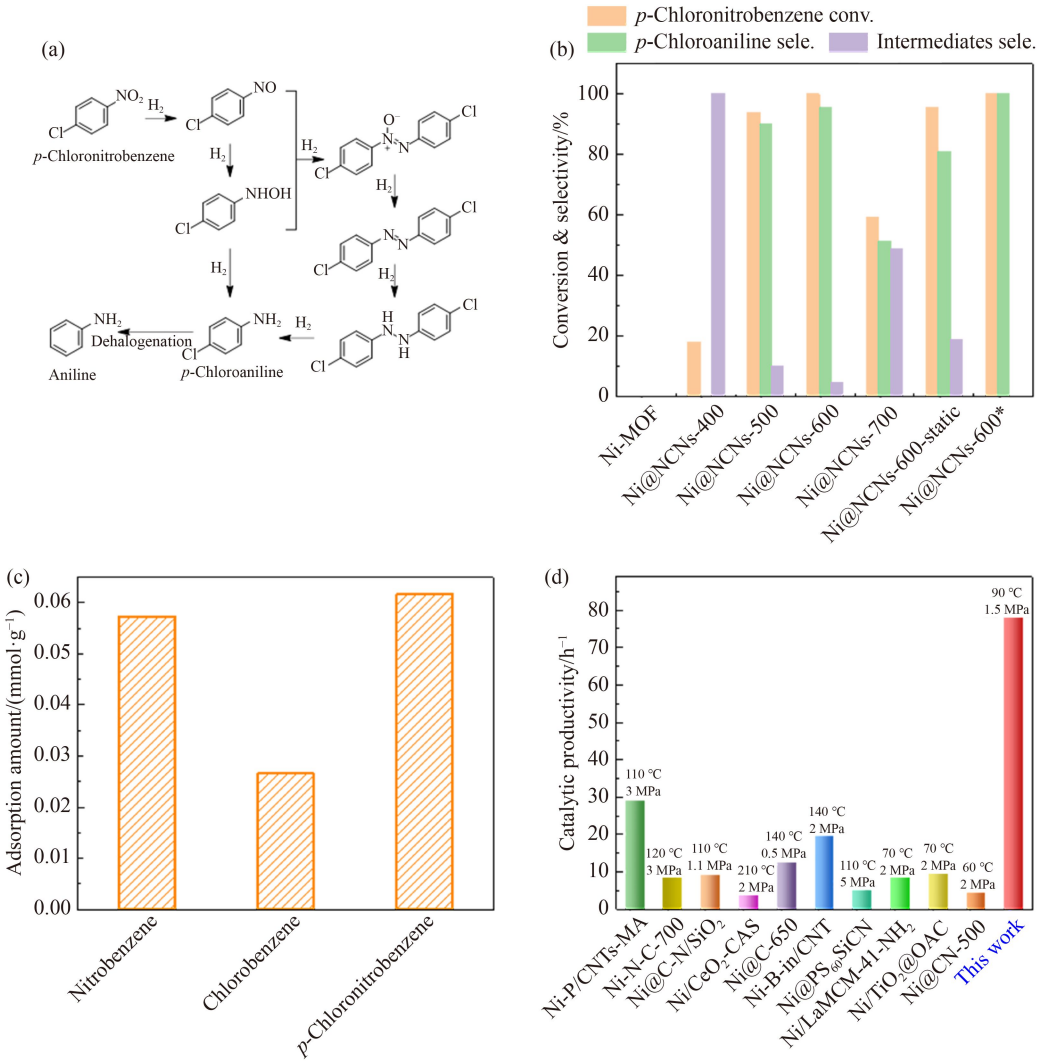

Fig. 5 (a) Proposed reaction routes for the hydrogenation of *p*-chloronitrobenzene. (b) Catalytic results of different catalysts for the selective hydrogenation of *p*-chloronitrobenzene to *p*-chloroaniline (reaction conditions: 53 mg *p*-chloronitrobenzene, 2.8 wt % equiv. catalyst, 2 mL ethanol, 80 °C, 2.0 MPa H_2, 60 min. * 787 mg *p*-chloronitrobenzene, 10 mg Ni@NCNs-600 catalyst, ethanol/H_2O (8/2, 10 mL), 90 °C, 1.5 MPa H_2, 60 min). (c) Saturated adsorption capacity of different substrates with Ni@NCNs-600. (d) Activity comparison of reported Ni-based catalysts for *p*-chloronitrobenzene hydrogenation to *p*-chloroaniline, the catalytic productivity is defined as the mole of converted *p*-chloronitrobenzene per mole of Ni per hour.

60 °C. As increasing temperature to 90 °C, full conversion and the highest selectivity (98.1%) were obtained. When the temperature was increased to 100 °C, 10.6% *p*-chloroaniline was dechlorinated. Therefore, 90 °C was chosen as the optimal temperature for the next exploration.

The effect of H_2 pressure was next investigated at 90 °C for 20 min (Fig. 6(c)). With 0.5 MPa H_2 pressure, only 29.0% conversion and 42.7% *p*-chloroaniline selectivity were observed. Increasing H_2 pressure to 1.0 MPa led to full conversion and 93.4% *p*-chloroaniline selectivity. The optimal *p*-chloroaniline yield (99.3%) was achieved at 1.5 MPa H_2, which was slightly higher than that obtained at 2.0 MPa H_2. Therefore, 1.5 MPa was the optimal H_2 pressure at 90 °C.

Nowadays, it is still challenging to develop non-noble metal catalysts that are still active enough at mild temperature or H_2 pressure. Surprisingly, Ni@NCNs-600 exhibited extraordinary performance and achieved 100% conversion and > 99% *p*-chloroaniline selectivity under 1.0–3.0 MPa H_2 at room temperature when prolonging reaction time to 20 h (Fig. 6(d)). Even decreasing H_2 pressure to 0.5 MPa, 57.3% conversion and 55.2% *p*-chloroaniline selectivity were still obtained.

To investigate the stability of Ni@NCNs-600 (Fig. 7), recycling test was carried out at 90 °C and 1.5 MPa for five successive runs (Fig. 7(a)). Thanks to the magnetic property of Ni@NCNs-600 derived from high Ni loading, it could be fully recovered by using a magnet and then applied for the next run without reduction. Until the fifth run, the *p*-chloronitrobenzene conversion was maintained at 100% and the *p*-chloroaniline selectivity was up to 92%, illustrating the outstanding recyclability of Ni@NCNs-600 (Fig. 7(a)). PXRD patterns (Fig. 7(b)) of

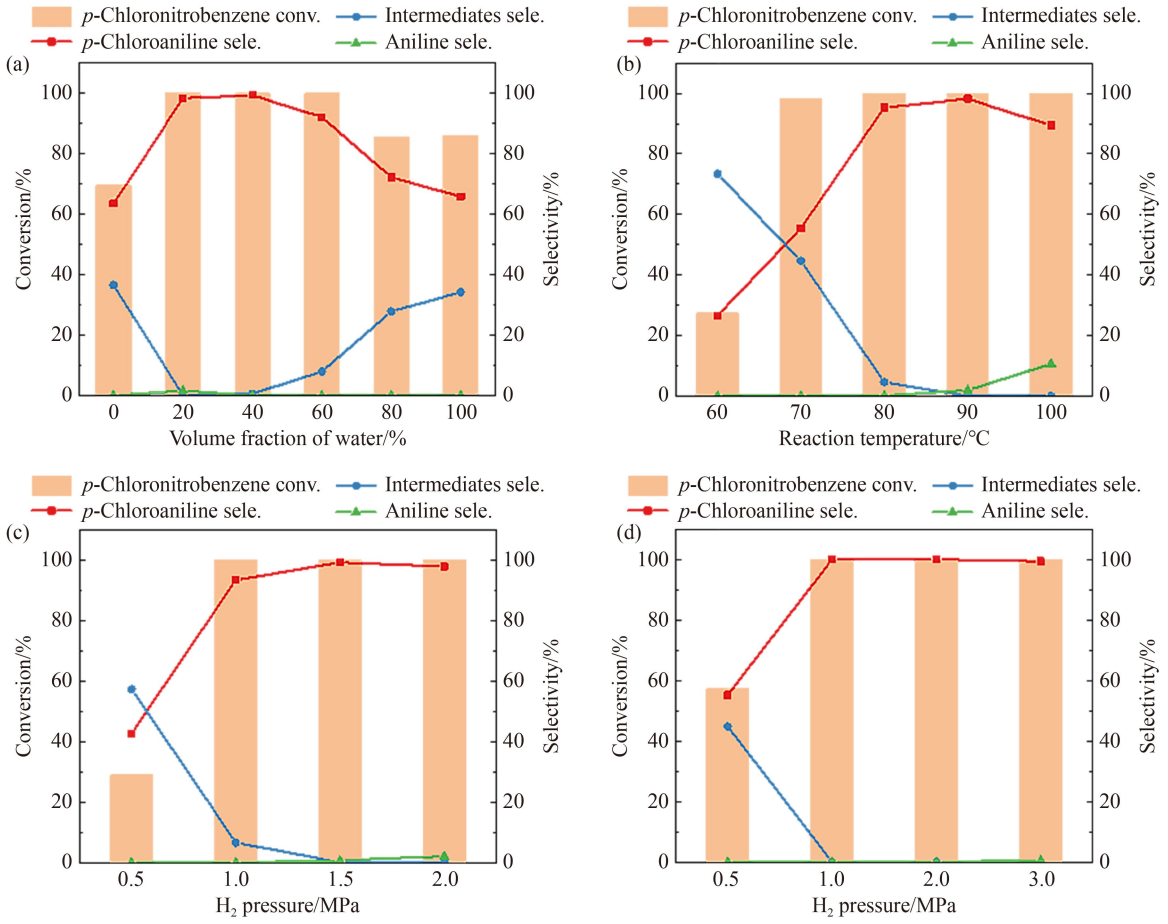

Fig. 6 (a) Effect of water on the hydrogenation of *p*-chloronitrobenzene (reaction conditions: 53 mg *p*-chloronitrobenzene, 2.8 wt % equiv. Ni@NCNs-600 catalyst, 2 mL solvent, 80 °C, 2.0 MPa H_2, 30 min). (b) Effect of reaction temperature on the hydrogenation of *p*-chloronitrobenzene (reaction conditions: 53 mg *p*-chloronitrobenzene, 2.8 wt % equiv. Ni@NCNs-600 catalyst, 2 mL solvent (ethanol/H_2O = 8/2), 2.0 MPa H_2, 20 min). (c) Effect of hydrogen pressure on the hydrogenation of *p*-chloronitrobenzene (reaction conditions: 53 mg *p*-chloronitrobenzene, 2.8 wt % equiv. Ni@NCNs-600 catalyst, 2 mL solvent (ethanol/H_2O = 8/2), 90 °C, 20 min). (d) Effect of hydrogen pressure on the room-temperature hydrogenation of *p*-chloronitrobenzene (reaction conditions: 53 mg *p*-chloronitrobenzene, 2.8 wt % equiv. Ni@NCNs-600 catalyst, 1.5 mL solvent (ethanol/H_2O = 8/2), room temperature, 20 h).

the spent catalyst display similar diffractions as the fresh one, indicating its good structure stability. To exclude the possible homogeneous catalysis, filtration test was performed (Fig. 7(c)). After 10 min, the reaction mixture was divided into two equal portions. For portion A, the catalyst was removed by filtration and no further conversion of *p*-chloronitrobenzene was observed. For portion B reserved with catalyst, the hydrogenation reaction continued and 93.7% *p*-chloroaniline yield was achieved after another 10 min, confirming the nature of heterogeneity.

Encouraged by the good performance of Ni@NCNs-600, we further explored its general applicability for selective hydrogenation of various sensitive-group-substituted nitroarenes (Table 1). It was found that the reaction proceeded with excellent activity and selectivity regardless of the halogen substituent located in ortho, meta, or para positions (Table 1, entries 1–5). For multi-halogen substituted nitrobenzene like 2,5-dibromonitrobenzene (Table 1, entry 6), the reaction could also achieve 94% conversion and 97% selectivity. Even for 4-iodonitrobenzene with a highly sensitive iodine group, full conversion and high selectivity (93%) could be achieved (Table 1, entry 7). In addition, other sensitive functional groups (e.g., –COOH, –$COCH_3$ and –CN) were well preserved under similar reaction conditions (Table 1, entries 8–10).

4 Conclusions

In summary, with stirring-crystallized di-ligands Ni-MOF as precursor, we developed ultra-dispersed Ni catalyst supported on Ni@NCNs via facile controllable pyrolysis, which was highly efficient for hydrogenation of halogenated nitroarenes to corresponding amines under mild conditions even at room temperature. Compared with the static-crystallized counterpart, stirring-crystallization produced smaller and uniform Ni-MOF

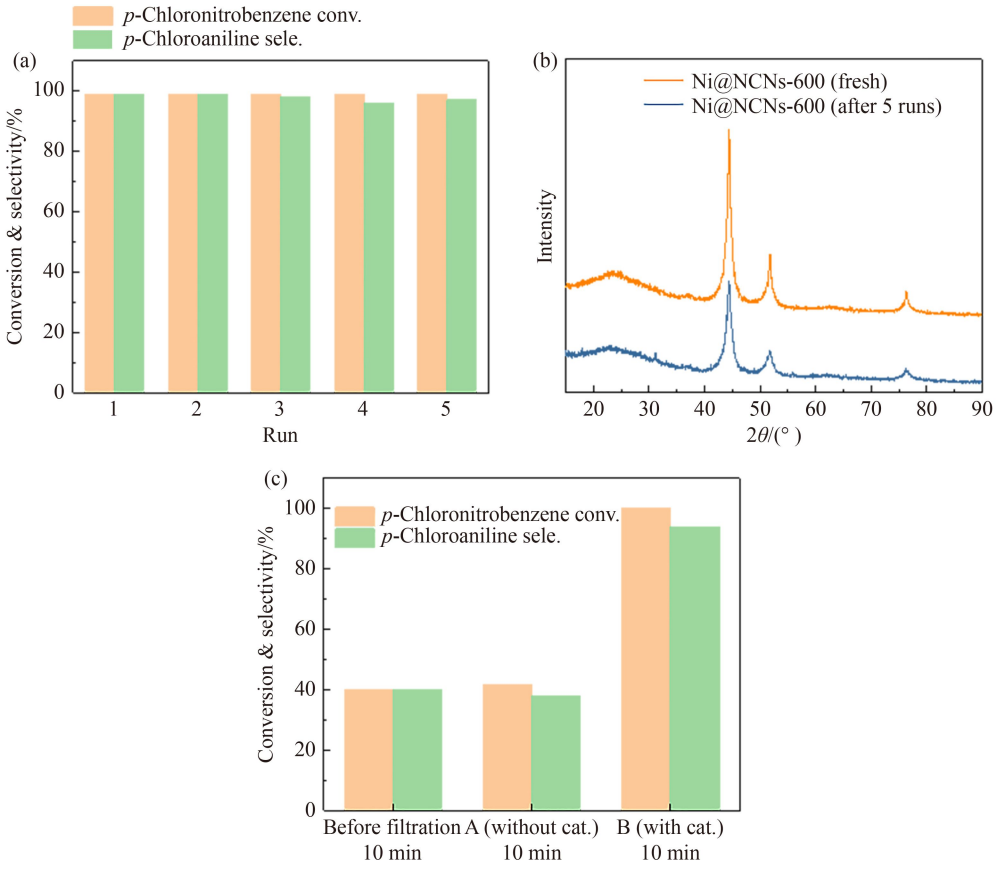

Fig. 7 (a) Recycling test of Ni@NCNs-600 in the hydrogenation of *p*-chloronitrobenzene (reaction conditions: 53 mg *p*-chloronitrobenzene, 2.8 wt % equiv. Ni@NCNs-600 catalyst, 2 mL solvent (ethanol/H_2O = 8/2), 90 °C, 1.5 MPa H_2, 20 min). (b) PXRD patterns of fresh and spent Ni@NCNs-600 catalysts. (c) The filtration experiment of Ni@NCNs-600 (reaction conditions: 53 mg *p*-chloronitrobenzene, 2.8 wt % equiv. Ni@NCNs-600 catalyst, 2 mL solvent (ethanol/H_2O = 8/2), 80 °C, 2 MPa H_2).

Table 1 Selective hydrogenation of various sensitive-group-substituted nitroarenes [a)]

Entry	Substrate	Product	Time/min	Conv./%	Sele./%
1	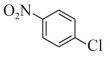	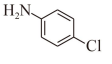	20	100	>99
2	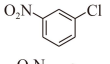	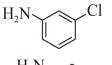	40	100	98
3			20	100	>99
4			20	100	97
5	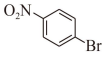	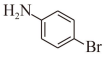	30	100	95
6	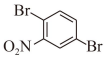	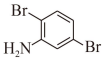	40	94	97
7[b)]			80	100	93
8	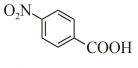	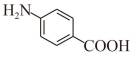	30	100	>99
9	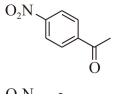	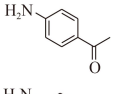	30	100	>99
10	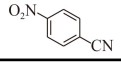	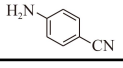	40	92	95

a) Reaction conditions: substrate (53 mg), 2.8 wt % equiv. Ni@NCNs-600 catalyst, ethanol/H_2O (8/2, 2 mL), 90 °C, 1.5 MPa H_2; b) substrate (24.9 mg).

nanoneedles, thus restraining Ni sintering during the pyrolysis. After systematic screening, the optimal Ni@NCNs-600 showed an extraordinarily high catalytic productivity of 77.9 h^{-1} and > 99% *p*-chloroaniline selectivity at full *p*-chloronitrobenzene conversion at 90 °C and 1.5 MPa H_2, which outperforms most reported Ni-based catalysts. Surprisingly, the *p*-chloroaniline hydrogenation could smoothly proceed at room temperature and 0.5 MPa H_2. The high activity can be attributed to high Ni dispersion, special morphology, and rich pore structure of the catalyst, while the high selectivity originates from its preferential adsorption of nitro group. Moreover, Ni@NCNs-600 was highly recyclable via magnetic separation and exhibited superior tolerance to various sensitive-group-substituted nitroarenes. This work opens a new vision for the design of MOF-derived non-noble metal catalysts with unique morphology and ultra-dispersion.

Acknowledgements This work was supported by the National Key R&D Program of China (Grant No. 2021YFC2103704), the National Natural Science Foundation of China (Grant Nos. 21878266 and 22078288), the Science and Technology Research Project of Henan Province (Grant No. 222300420527), and Program of Processing and Efficient Utilization of Biomass Resources of Henan Center for Outstanding Overseas Scientists (Grant No. GZS2022007).

Electronic Supplementary Material Supplementary material is available in the online version of this article at http://dx.doi.org/10.1007/s11705-022-2220-9 and is accessible for authorized users.

References

1. Formenti D, Ferretti F, Scharnagl F K, Beller M. Reduction of nitro compounds using 3d-non-noble metal catalysts. Chemical Reviews, 2019, 119(4): 2611–2680
2. Trandafir M M, Neatu F, Chirica I M, Neatu S, Kuncser A C, Cucolea E I, Natu V, Barsoum M W, Florea M. Highly efficient ultralow Pd loading supported on MAX phases for chemoselective hydrogenation. ACS Catalysis, 2020, 10(10): 5899–5908
3. Song J, Huang Z, Pan L, Li K, Zhang X, Wang L, Zou J. Review on selective hydrogenation of nitroarene by catalytic, photocatalytic and electrocatalytic reactions. Applied Catalysis B: Environmental, 2018, 227: 386–408
4. Wei H, Liu X, Wang A, Zhang L, Qiao B, Yang X, Huang Y, Miao S, Liu J, Zhang T. FeO_x-supported platinum single-atom and pseudo-single-atom catalysts for chemoselective hydrogenation of functionalized nitroarenes. Nature Communications, 2014, 5(1): 5634
5. Westerhaus F A, Jagadeesh R V, Wienhofer G, Pohl M M, Radnik J, Surkus A E, Rabeah J, Junge K, Junge H, Nielsen M, Brückner A, Beller M. Heterogenized cobalt oxide catalysts for nitroarene reduction by pyrolysis of molecularly defined complexes. Nature Chemistry, 2013, 5(6): 537–543
6. Jagadeesh R V, Surkus A E, Junge H, Pohl M M, Radnik J, Rabeah J, Huan H, Schunemann V, Bruckner A, Beller M. Nanoscale Fe_2O_3-based catalysts for selective hydrogenation of nitroarenes to anilines. Science, 2013, 342(6162): 1073–1076
7. Sankar M, Dimitratos N, Miedziak P J, Wells P P, Kiely C J, Hutchings G J. Designing bimetallic catalysts for a green and sustainable future. Chemical Society Reviews, 2012, 41(24): 8099–8139
8. Gao C, Lyu F, Yin Y. Encapsulated metal nanoparticles for catalysis. Chemical Reviews, 2021, 121(2): 834–881
9. Munnik P, de Jongh P E, de Jong K P. Recent developments in the synthesis of supported catalysts. Chemical Reviews, 2015, 115(14): 6687–6718
10. Yang X, Liu W, Tan F, Zhang Z, Chen X, Liang T, Wu C. A robust strategy of homogeneously hybridizing silica and $Cu_3(BTC)_2$ to *in situ* synthesize highly dispersed copper catalyst for furfural hydrogenation. Applied Catalysis A: General, 2020, 596: 117518
11. Li J, Wang B, Qin Y, Tao Q, Chen L. MOF-derived Ni@NC catalyst: synthesis, characterization, and application in one-pot hydrogenation and reductive amination. Catalysis Science & Technology, 2019, 9(14): 3726–3734
12. Su D, Perathoner S, Centi G. Nanocarbons for the development of advanced catalysts. Chemical Reviews, 2013, 113(8): 5782–5816
13. Wang J, Kong H, Zhang J, Hao Y, Shao Z, Ciucci F. Carbon-based electrocatalysts for sustainable energy applications. Progress in Materials Science, 2021, 116: 100717
14. Shi Z, Yang W, Gu Y, Liao T, Sun Z. Metal-nitrogen-doped carbon materials as highly efficient catalysts: progress and rational design. Advanced Science, 2020, 7(15): 2001069
15. Zhang Q, Zhang D, Zhou Y, Qian J, Wen X, Jiang P, Ma L, Lu C, Feng F, Li X. Preparation of heteroatom-doped carbon materials and applications in selective hydrogenation. ChemistrySelect, 2022, 7(4): e202102581
16. Yang J, Li W, Wang D, Li Y. Electronic metal-support interaction of single-atom catalysts and applications in electrocatalysis. Advanced Materials, 2020, 32(49): 2003300
17. Shen K, Chen X, Chen J, Li Y. Development of MOF-derived carbon-based nanomaterials for efficient catalysis. ACS Catalysis, 2016, 6(9): 5887–5903
18. Wang Q, Astruc D. State of the art and prospects in metal–organic framework (MOF)-based and MOF-derived nanocatalysis. Chemical Reviews, 2020, 120(2): 1438–1511
19. Wang J, Wang Y, Hu H, Yang Q, Cai J. From metal-organic frameworks to porous carbon materials: recent progress and prospects from energy and environmental perspectives. Nanoscale, 2020, 12(7): 4238–4268
20. He Y, Wang Z, Wang H, Wang Z, Zeng G, Xu P, Huang D, Chen M, Song B, Qin H, Zhao Y. Metal–organic framework-derived nanomaterials in environment related fields: fundamentals, properties and applications. Coordination Chemistry Reviews, 2021, 429: 213618
21. Hu W, Zheng M, Xu B, Wei Y, Zhu W, Li Q, Pang H. Design of hollow carbon-based materials derived from metal–organic frameworks for electrocatalysis and electrochemical energy storage. Journal of Materials Chemistry A: Materials for Energy and Sustainability, 2021, 9(7): 3880–3917

22. Lakhi K S, Park D H, Al-Bahily K, Cha W, Viswanathan B, Choy J H, Vinu A. Mesoporous carbon nitrides: synthesis, functionalization, and applications. Chemical Society Reviews, 2017, 46(1): 72–101
23. Wang C, Kim J, Tang J, Kim M, Lim H, Malgras V, You J, Xu Q, Li J, Yamauchi Y. New strategies for novel MOF-derived carbon materials based on nanoarchitectures. Chem, 2020, 6(1): 19–40
24. Cheng N, Ren L, Xu X, Du Y, Dou S X. Recent development of zeolitic imidazolate frameworks (ZIFs) derived porous carbon based materials as electrocatalysts. Advanced Energy Materials, 2018, 8(25): 1801257
25. Song X, Jiang Y, Cheng F, Earnshaw J, Na J, Li X, Yamauchi Y. Hollow carbon-based nanoarchitectures based on ZIF: inward/outward contraction mechanism and beyond. Small, 2021, 17(2): 2004142
26. Han J, Meng X, Lu L, Bian J, Li Z, Sun C. Single-atom Fe–N_x–C as an efficient electrocatalyst for zinc-air batteries. Advanced Functional Materials, 2019, 29(41): 1808872
27. Fan Y, Zhuang C, Li S, Wang Y, Zou X, Liu X, Huang W, Zhu G. Efficient single-atom Ni for catalytic transfer hydrogenation of furfural to furfuryl alcohol. Journal of Materials Chemistry A: Materials for Energy and Sustainability, 2021, 9(2): 1110–1118
28. Huang L, Lv Y, Wu S, Liu P, Xiong W, Hao F, Luo H. Activated carbon supported bimetallic catalysts with combined catalytic effects for aromatic nitro compounds hydrogenation under mild conditions. Applied Catalysis A: General, 2019, 577: 76–85
29. Wang J, Fan G, Li F. A hybrid nanocomposite precursor route to synthesize dispersion-enhanced Ni catalysts for the selective hydrogenation of *o*-chloronitrobenzene. Catalysis Science & Technology, 2013, 3(4): 982–991
30. Zhang P, Zhao Z, Dyatkin B, Liu C, Qiu J. *In situ* synthesis of cotton-derived Ni/C catalysts with controllable structures and enhanced catalytic performance. Green Chemistry, 2016, 18(12): 3594–3599
31. Pan H, Peng Y, Lu X, He J, He L, Wang C, Yue F, Zhang H, Zhou D, Xia Q. Well-constructed Ni@CN material derived from di-ligands Ni-MOF to catalyze mild hydrogenation of nitroarenes. Molecular Catalysis, 2020, 485: 110838
32. Li G, Yang H, Zhang H, Qi Z, Chen M, Hu W, Tian L, Nie R, Huang W. Encapsulation of nonprecious metal into ordered mesoporous N-doped carbon for efficient quinoline transfer hydrogenation with formic acid. ACS Catalysis, 2018, 8(9): 8396–8405
33. Luo Z, Nie R, Nguyen V T, Biswas A, Behera R K, Wu X, Kobayashi T, Sadow A, Wang B, Huang W, Qi L. Transition metal-like carbocatalyst. Nature Communications, 2020, 11(1): 4091
34. Tao Y, Nie Y, Hu H, Wang K, Chen Y, Nie R, Wang J, Lu T, Zhang Y, Xu C C. Highly active Ni nanoparticles on N-doped mesoporous carbon with tunable selectivity for the one-pot transfer hydroalkylation of nitroarenes with EtOH in the absence of H_2. ChemCatChem, 2021, 13(19): 4243–4250
35. Murugesan K, Alshammari A S, Sohail M, Beller M, Jagadeesh R V. Monodisperse nickel-nanoparticles for stereo- and chemoselective hydrogenation of alkynes to alkenes. Journal of Catalysis, 2019, 370: 372–377
36. Murugesan K, Beller M, Jagadeesh R V. Reusable nickel nanoparticles-catalyzed reductive amination for selective synthesis of primary amines. Angewandte Chemie International Edition, 2019, 58(15): 5064–5068
37. Yang F, Wang M, Liu W, Yang B, Wang Y, Luo J, Tang Y, Hou L, Li Y, Li Z, Zhang B, Yang W, Li Y. Atomically dispersed Ni as the active site towards selective hydrogenation of nitroarenes. Green Chemistry, 2019, 21(3): 704–711
38. Li S, Chen X, Wang J, Yao N, Wang J, Cen J, Li X. Construction the Ni@carbon nanostructure with dual-reaction surfaces for the selective hydrogenation reaction. Applied Surface Science, 2019, 489: 786–795
39. Li F, Ma R, Cao B, Liang J, Song H, Song H. Effect of loading method on selective hydrogenation of chloronitrobenzenes over amorphous Ni-B/CNTs catalysts. Catalysis Communications, 2016, 80: 1–4
40. She W, Qi T, Cui M, Yan P, Ng S W, Li W, Li G. High catalytic performance of a CeO_2-supported Ni catalyst for hydrogenation of nitroarenes, fabricated via coordination-assisted strategy. ACS Applied Materials & Interfaces, 2018, 10(17): 14698–14707
41. Kang Y, Du H, Jiang B, Li H, Guo Y, Amin M A, Sugahara Y, Asahi T, Li H, Yamauchi Y. Microwave one-pot synthesis of CNT-supported amorphous Ni−P alloy nanoparticles with enhanced hydrogenation performance. Journal of Materials Chemistry A: Materials for Energy and Sustainability, 2022, 10(12): 6560–6568
42. Tang B, Song W, Yang E, Zhao X. MOF-derived Ni-based nanocomposites as robust catalysts for chemoselective hydrogenation of functionalized nitro compounds. RSC Advances, 2017, 7(3): 1531–1539
43. Huang L, Lv Y, Liu S, Cui H, Zhao Z, Zhao H, Liu P, Xiong W, Hao F, Luo H. Non-noble metal Ni nanoparticles supported on highly dispersed TiO_2-modified activated carbon as an efficient and recyclable catalyst for the hydrogenation of halogenated aromatic nitro compounds under mild conditions. Industrial & Engineering Chemistry Research, 2020, 59(4): 1422–1435
44. Hahn G, Ewert J K, Denner C, Tilgner D, Kempe R. A reusable mesoporous nickel nanocomposite catalyst for the selective hydrogenation of nitroarenes in the presence of sensitive functional groups. ChemCatChem, 2016, 8(15): 2461–2465
45. Huang L, Tang F, Hao F, Zhao H, Liu W, Lv Y, Liu P, Xiong W, Luo H. Tuning the electron density of metal nickel via interfacial electron transfer in Ni/MCM-41 for efficient and selective catalytic hydrogenation of halogenated nitroarenes. ACS Sustainable Chemistry & Engineering, 2022, 10(9): 2947–2959
46. Wang H, Wang Y, Li Y, Lan X, Ali B, Wang T. Highly efficient hydrogenation of nitroarenes by N-doped carbon-supported cobalt single-atom catalyst in ethanol/water mixed solvent. ACS Applied Materials & Interfaces, 2020, 12(30): 34021–34031
47. Li M, Chen S, Jiang Q, Chen Q, Wang X, Yan Y, Liu J, Lv C, Ding W, Guo X. Origin of the activity of Co–N–C catalysts for chemoselective hydrogenation of nitroarenes. ACS Catalysis, 2021, 11(5): 3026–3039
48. Li G, Wang B, Resasco D E. Water-mediated heterogeneously catalyzed 48. reactions. ACS Catalysis, 2019, 10(2): 1294–1309